Supplemental

Contents:

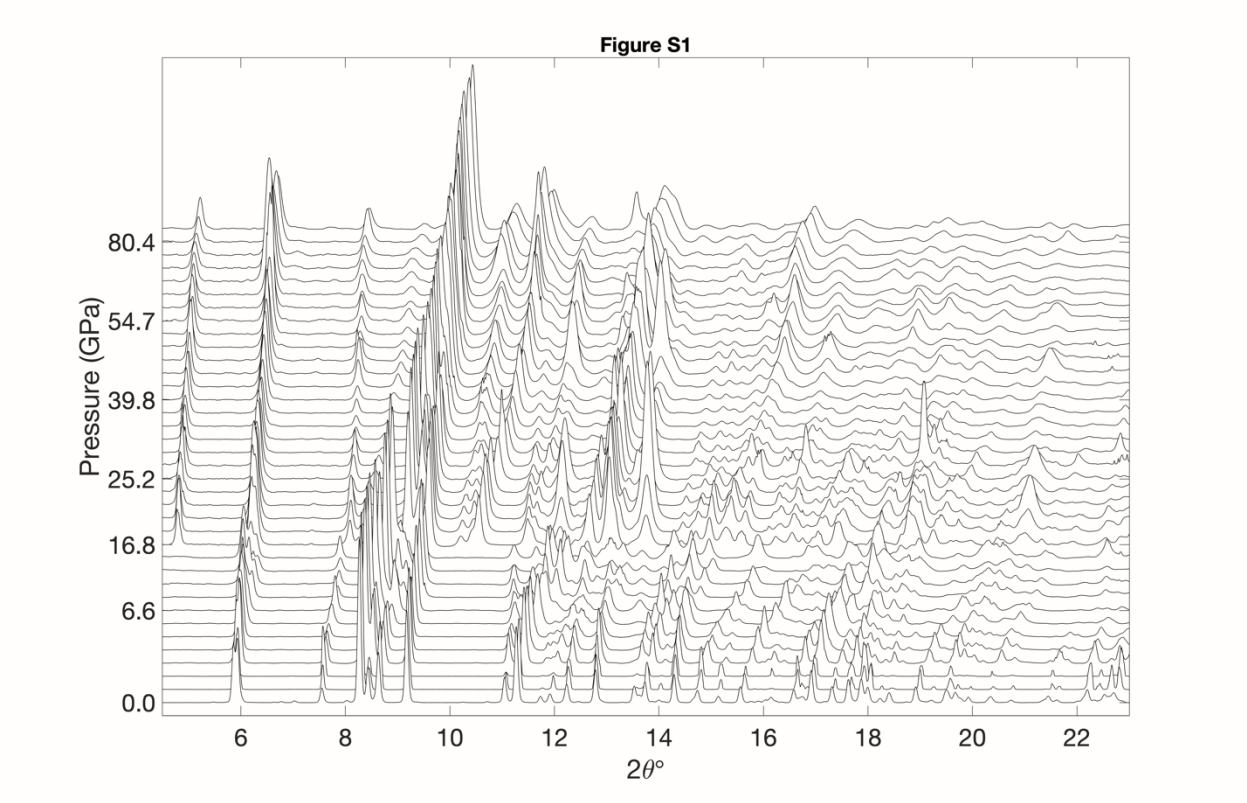

Figure S1. Each pattern has undergone background removal and normalization such that the maximum intensity is equal to one. Each pattern has been plotted as a function of 2θ and set to a uniform height. Patterns are stacked vertically with pressure increasing along the y-axis.

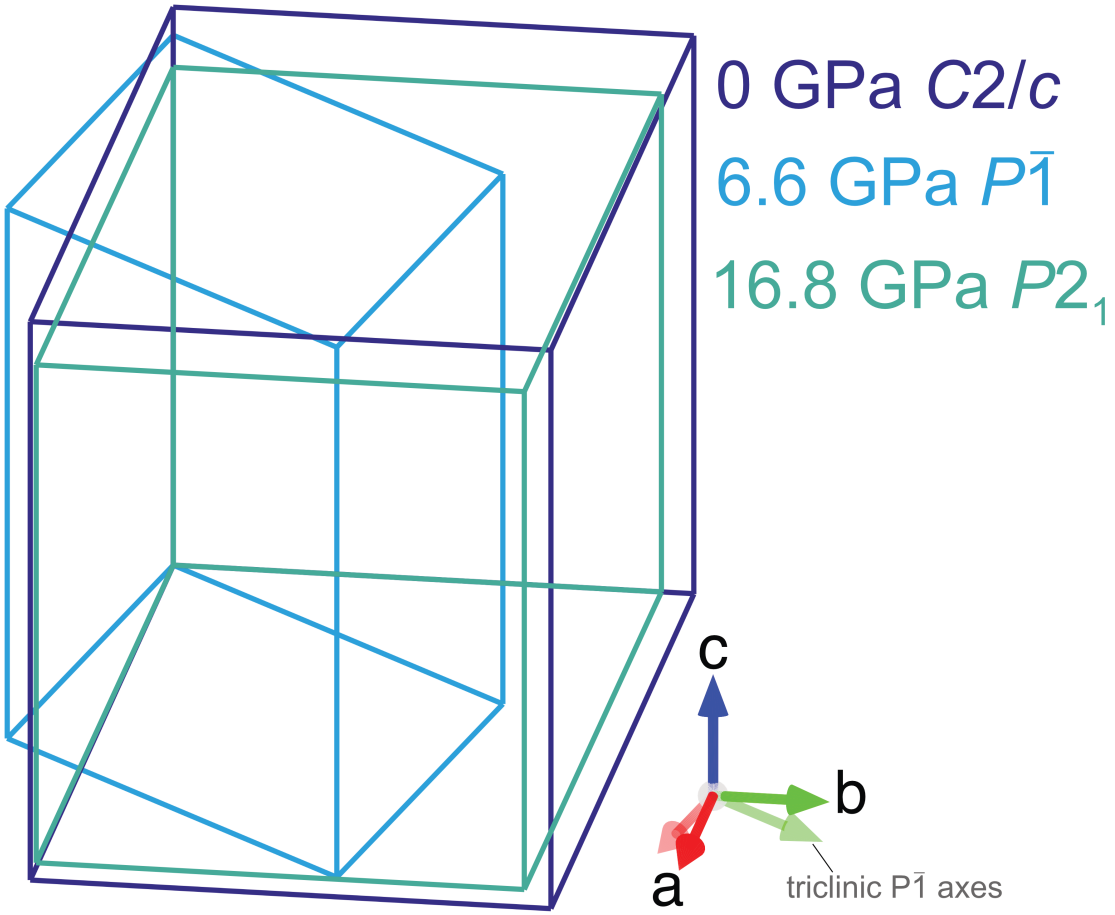

Figure S2: Relative unit cell size and orientation of the three space groups identified within our experimental pressure regime at the lowest pressure of stability. Cells are centered with the assumption that corner Fe-atoms are at the origin. Note the orientation difference between the monoclinic space groups and the mid-pressure triclinic space group. This difference in size and orientation motivates the transformation of the triclinic lattice to a monoclinic setting such that angles α and β are ~90º and the monoclinic setting volume is exactly twice the volume of the triclinic setting. This transformation was carried out using the transformation matrix from Giester et al. 1994 following Meusburger et al. 2019.

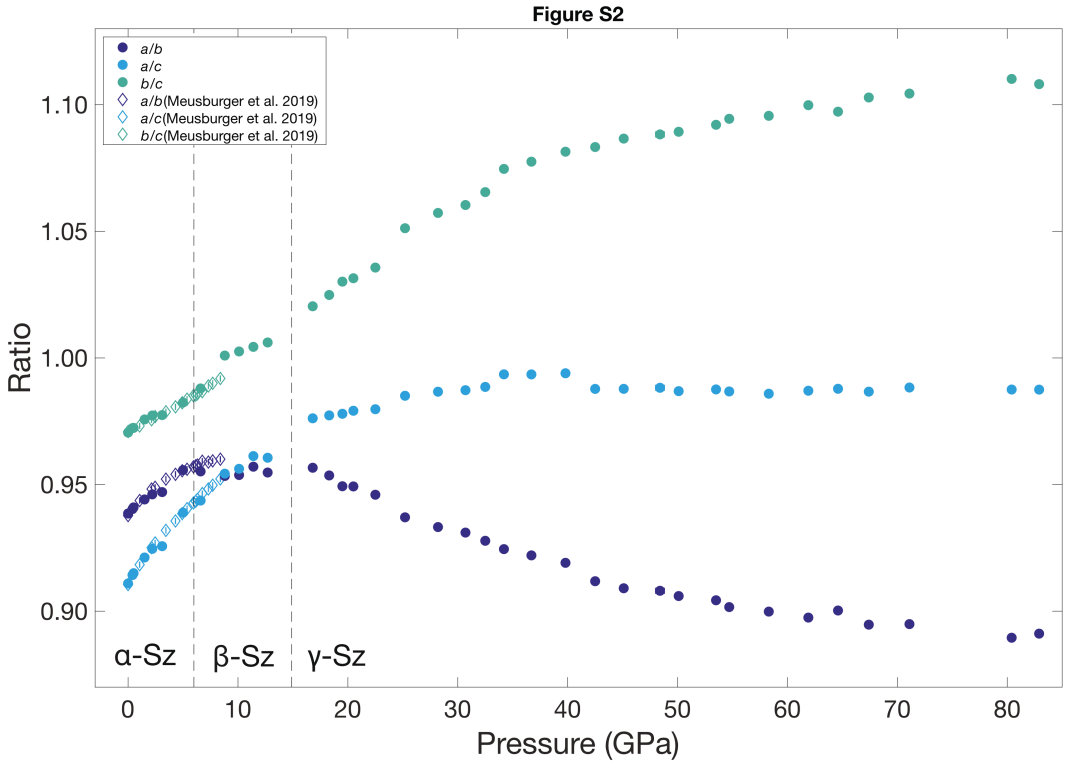

Figure S3: Axial ratios *a*/*b*, *a*/*c*, and *b*/*c* are plotted as a function of pressure for this study as well as those reported by Meusburger et al. (2019). The *b*/*c* ratio continues to increase across the entire pressure range of this experiment. The *a*/*b* ratio increases, then plateaus in the triclinic stability field. After the *P*-1 to $P2_1$ transition, the *a*/*b* ratio decreases until the last pressure measured. The *a*/*c* ratio increases until plateauing at ~20 GPa.

Figure S4

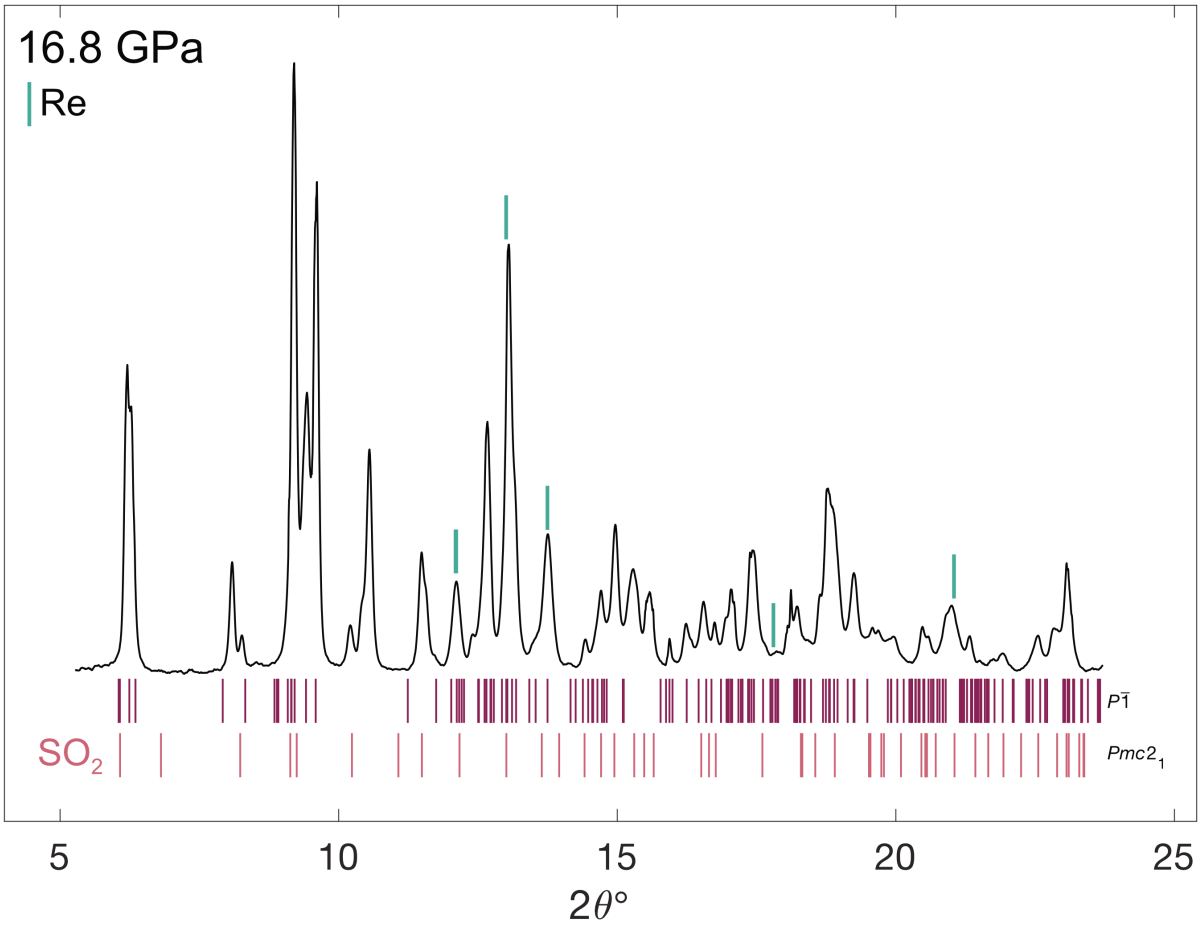

Figure S4. 16.8 GPa XRD pattern assuming that at this pressure szomolnokite remains in the triclinic *P*-1 phase with the addition of SO_2. Reflections of high pressure SO_2 are taken from a theoretical study by Zhang et al. 2020. Note the absence of reflection corresponding to the new peaks at ~10.5º 2θ.

Figure S5

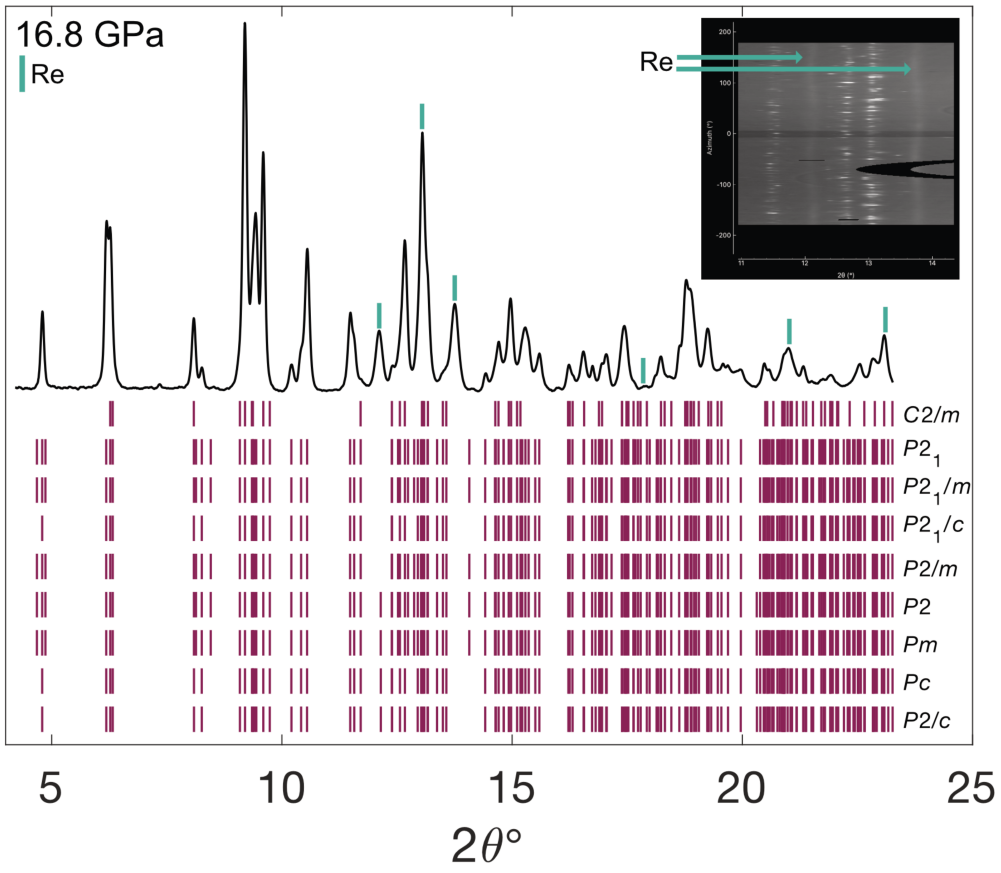

Figure S5. 16.8 GPa XRD pattern with eight candidate primitive monoclinic space groups and one face-centered space group: *C*2/*m*, *P*2$_1$, *P*2$_1$/*m*, *P*2/*m*, *P*2/*c, P*2$_1$/*c, P*2, *Pm*, and *Pc.* The *C*2/*m* space group lacks reflections associated with the new peaks at this pressure including peaks at ~5º and ~11º 2θ. Re peaks are indicated as the green reflections located above each Re peak. Top right inset shows the raw image zoomed into ~11º-14º 2θ. Green arrows point to the isolated Re peaks.

Figure S6

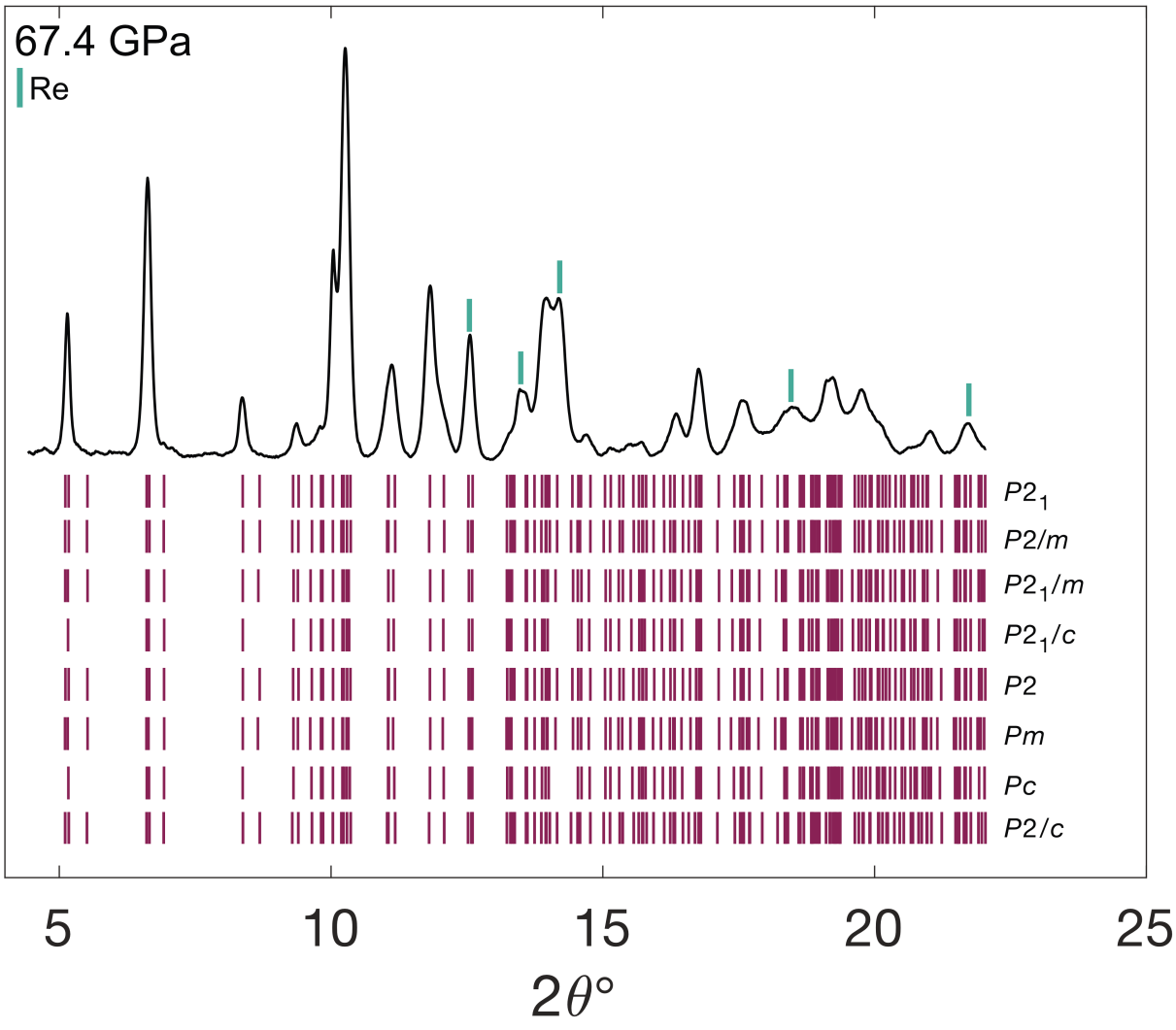

Figure S6. 67.4 GPa XRD pattern with eight candidate primitive monoclinic space groups $P2_1$, $P2_1/m$, $P2/m$, $P2/c$, $P2_1/c$, $P2$, Pm, and Pc. Re peaks are indicated as the green reflections located above each Re peak.

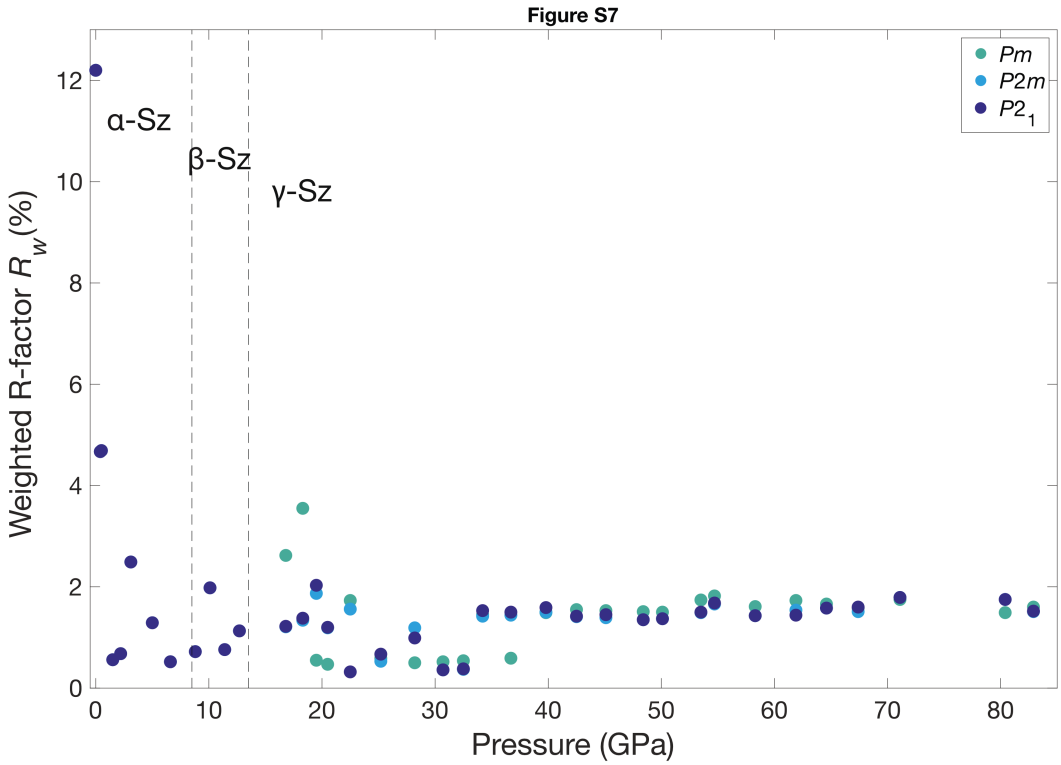

Figure S7. GSAS-II calculates a weighted R-factor (R_w) value useful for comparing different structural fits to a given data set. This factor was not used in place of a visual assessment of structural refinements to the data. The R_w values were used in this study as an additional comparison of competing structural refinements for the new, high-pressure structural transition. Plotted here are three examples of R_w values for the $P2_1$, $P2/m$, and Pm phases. For reasons explained in detail in the main text (including absence of reflections overlapping with Re), the $P2_1$ space group was chosen as the γ-Sz space group. However, R_w values for all three space groups remain approximately constant over the entire pressure range of the γ-Sz phase, with the Pm being slightly more scattered than the other two near 20 GPa. Given the many overlapping low-intensity peaks at higher 2θ values (see Figure S1), the consistency in R_w values at high pressures indicates that several primitive monoclinic space groups can at least fit the high

intensity peaks well up to 83 GPa. The room-pressure R_w value is an outlier due to the high signal-to-background ratio, which generally results in artificially high R_w values (for a detailed discussion on R-factors see Toby (2006)). This room-pressure value was measured on powdered szomolnokite loaded in a Kapton tube and thus lacks X-ray diffraction background contribution from the diamonds due to Compton scattering.

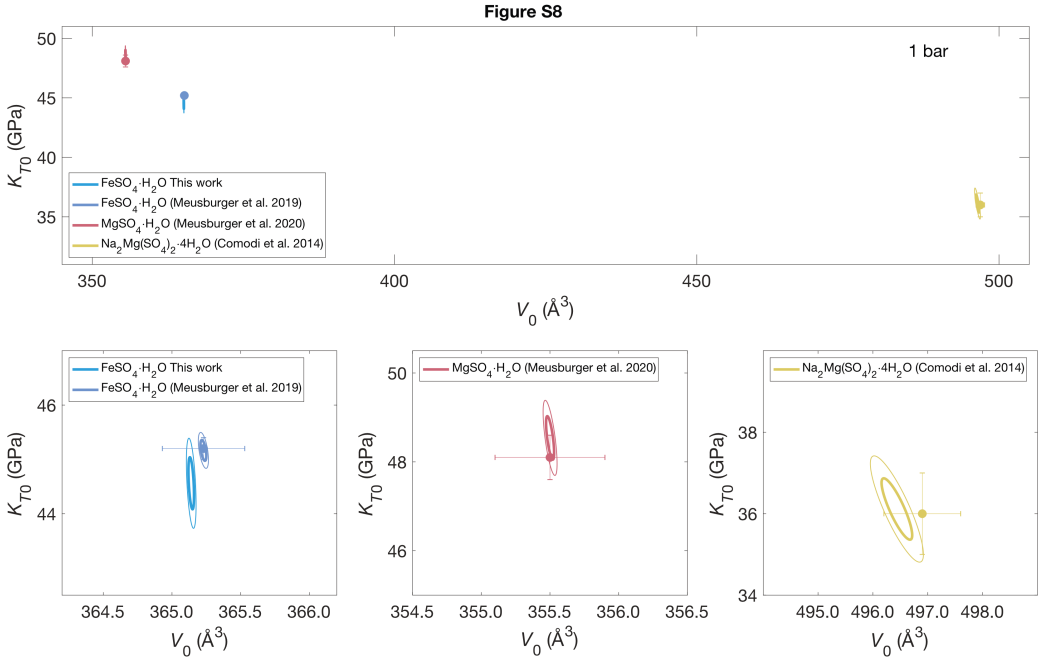

Figure S8: 1σ and 3σ K_{T0} vs. V_{T0} error ellipses for $FeSO_4·H_2O$, $MgSO_4·H_2O$, and $Na_2Mg(SO_4)_2·4H_2O$ at 1 bar.

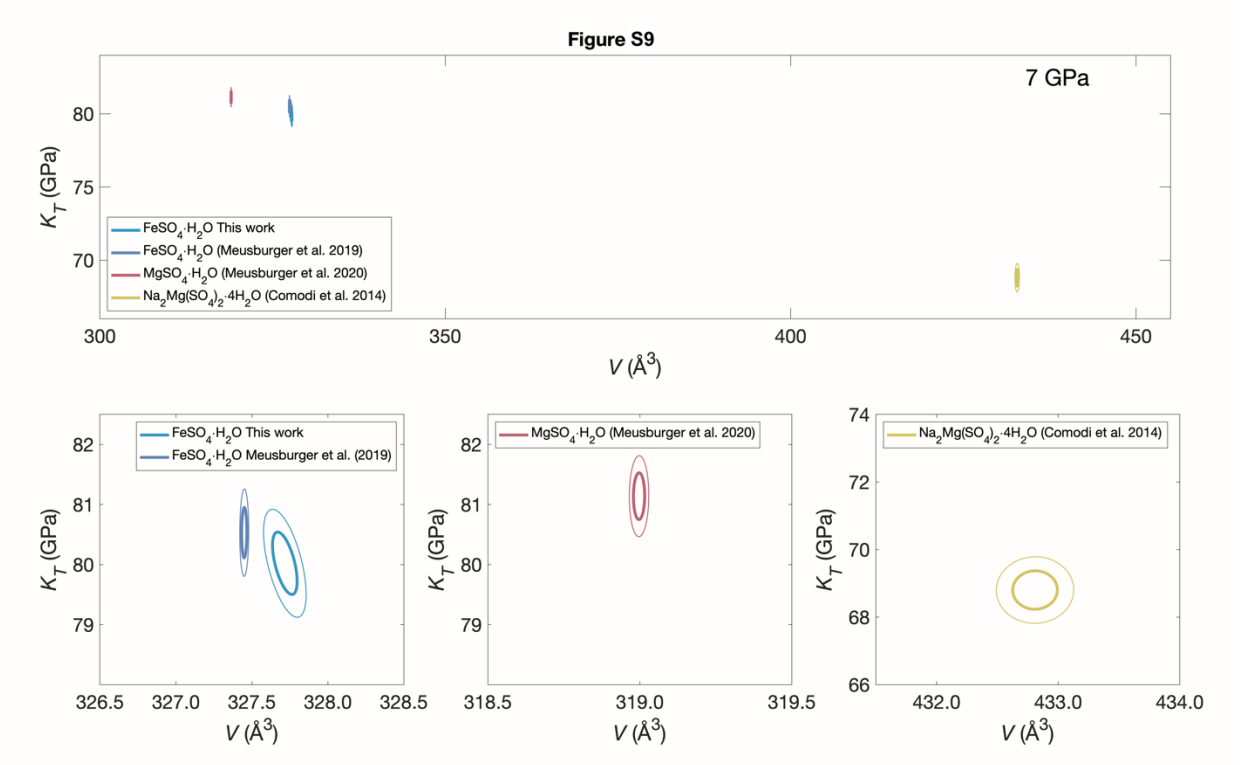

Figure S9: 1σ and 3σ K_T vs. V_T error ellipses for $FeSO_4·H_2O$, $MgSO_4·H_2O$, and $Na_2Mg(SO_4)_2·4H_2O$ at 7 GPa.

Figure S10

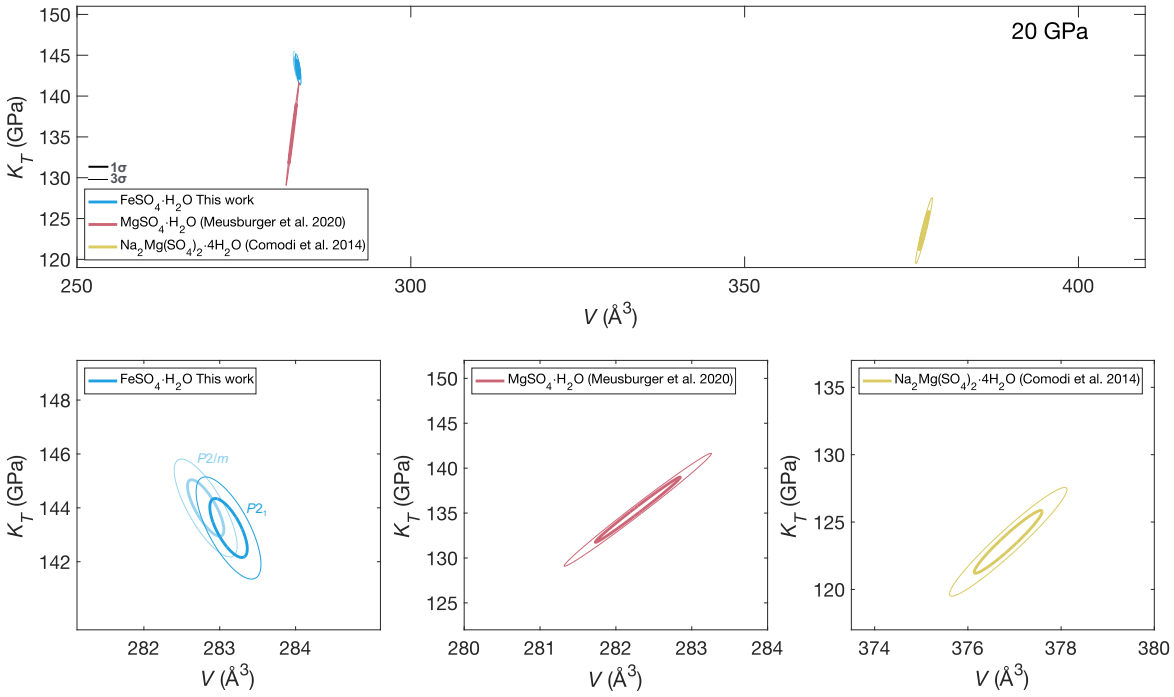

Figure S10: 1σ and 3σ K_T vs. V_T error ellipses for $FeSO_4 \cdot H_2O$, $MgSO_4 \cdot H_2O$, and $Na_2Mg(SO_4)_2 \cdot 4H_2O$ at 20 GPa. Both the $P2_1$ and $P2/m$ space group high-pressure EoS parameters are plotted for comparison and are the same within error.

Figure S11

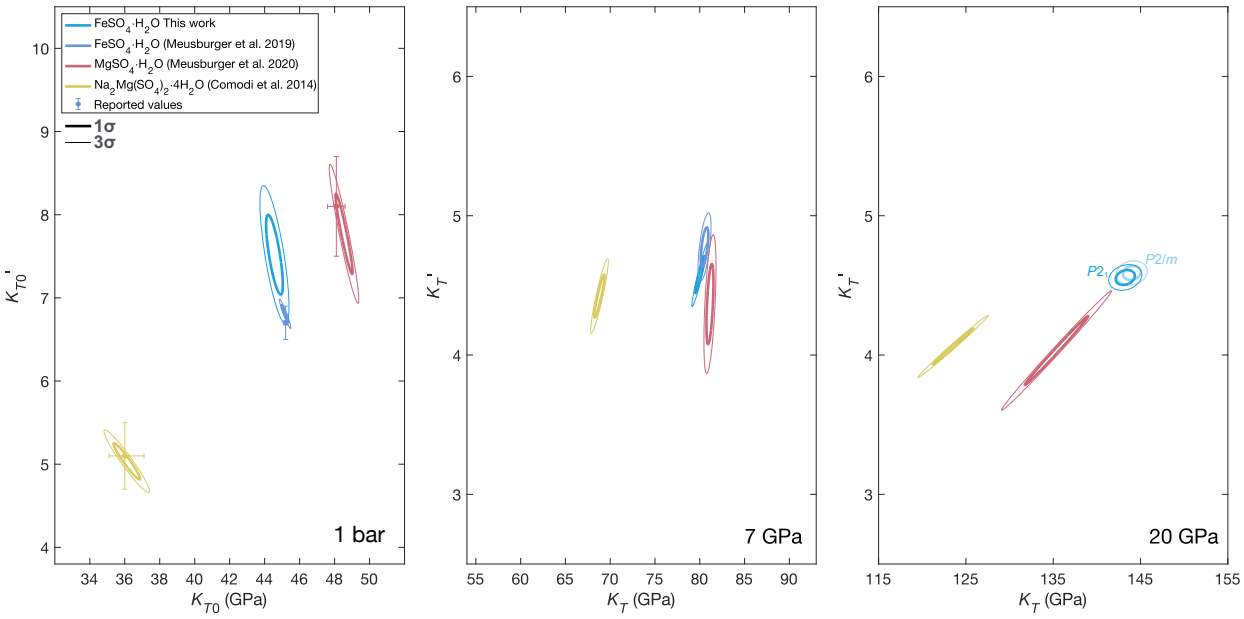

Figure S11: 1σ and 3σ K_T' vs. K_T error ellipses for $FeSO_4 \cdot H_2O$, $MgSO_4 \cdot H_2O$, and $Na_2Mg(SO_4)_2 \cdot 4H_2O$ at 1 bar, 7, and 20 GPa GPa, including $P2_1$ vs. $P2/m$ comparison in the far right panel at 20 GPa which have the same values within error.

References Cited

Giester, G., Lengauer, C.L., and Redhammer, G.J. (1994) Characterization of the $FeSO_4 \cdot H_2O$-$CuSO_4 \cdot H_2O$ solid-solution series, and the nature of poitevinite, $(Cu,Fe)SO_4 \cdot H_2O$. The Canadian Mineralogist, 32, 873–884.

Meusburger, J.M., Ende, M., Talla, D., Wildner, M., and Miletich, R. (2019) Transformation mechanism of the pressure-induced *C*2/*c*-to-*P*-1 transition in ferrous sulfate monohydrate single crystals. Journal of Solid State Chemistry, 277, 240–252.

Toby, B.H. (2006) R factors in Rietveld analysis: How good is good enough? Powder Diffraction, 21, 67–70.

Zhang, H., Tóth, O., Liu, X.-D., Bini, R., Gregoryanz, E., Dalladay-Simpson, P., De Panfilis, S., Santoro, M., Gorelli, F.A., and Martoňák, R. (2020) Pressure-induced amorphization and existence of molecular and polymeric amorphous forms in dense SO_2. Proceedings of the National Academy of Sciences, 117, 8736–8742.